ACS Photonics

pubs.acs.org/journal/apchd5

Article

Vacuum-Deposited Microcavity Perovskite Photovoltaic Devices

Abhyuday Paliwal, Chris Dreessen, Kassio P. S. Zanoni, Benedikt Dänekamp, Beom-Soo Kim, Michele Sessolo, Koen Vandewal, and Henk J. Bolink*

Cite This: *ACS Photonics* 2021, 8, 2067−2073

Read Online

ACCESS | Metrics & More | Article Recommendations | Supporting Information

ABSTRACT: The interaction between semiconductor materials and electromagnetic fields resonating in microcavities or the light−matter coupling is of both fundamental and practical significance for improving the performance of various photonic technologies. The demonstration of light−matter coupling effects in the emerging perovskite-based optoelectronic devices via optical pumping and electrical readout (e.g., photovoltaics) and vice versa (e.g., light-emitting diodes), however, is still scarce. Here, we demonstrate the microcavity formation in vacuum-deposited methylammonium lead iodide ($CH_3NH_3PbI_3$, MAPI) p-i-n photovoltaic devices fabricated between two reflecting silver electrodes. We tune the position of the microcavity mode across MAPI's absorption edge and study the effect on the microcavity absorption enhancement. Tuning the microcavity mode toward lower energies enhances the absorption of the lower energy photons and steepens the absorption onset which reduces the effective optical gap (E_g) of the devices. This leads to a reduction in the open circuit voltage deficit.

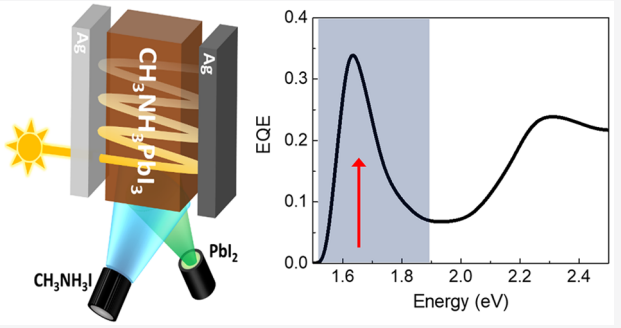

KEYWORDS: *light−matter coupling, microcavity device, hybrid organic inorganic perovskite, vacuum deposition, photovoltaic*

The integration of a semiconductor material into a microcavity device architecture offers an attractive avenue to enhance its properties and performance in various optoelectronic applications.[1] The above enhancement is generated by light−matter interactions operating under the strong or weak coupling regime. In the strong coupling regime, the coherent exchange of energy between the excited state and the microcavity mode leads to the formation of hybridized light−matter quasi-particles called polaritons, which possess different energies than the uncoupled resonant photonic mode and excited state.[2] In the weak coupling regime, the rate of exchange of energy between the exciton mode and the microcavity mode is lower than that of the dissipation processes. As a result, the weak coupling primarily alters the distribution of the optical density of states in the microcavity volume. The optical density of states at the microcavity mode are increased, which causes enhanced absorption (emission) of the resonant photonic mode in (from) the coupled semiconductor material.[3,4] The above modulation of the optical density of states can be strategically exploited to achieve spectrum selective photoabsorption in thin, low absorbing films, which is beneficial for narrow-linewidth photodetector application,[5] or to enhance the absorption of light at the weakly absorbing absorption-edge-region of the embedded semiconductor material, which is favorable for photovoltaic application.[3]

Lead halide perovskite materials are currently considered for various optoelectronic applications due to their exceptional material properties such as low charge carrier recombination, ambipolar charge transport, high charge carrier mobility, and band gap tunability, as well as strong light absorption across the visible spectrum and efficient photoluminescence.[6] Their high oscillator strength, sharp absorption-edge, small Stokes shift, and low Auger recombination losses make them attractive for exploring the advantages of light−matter coupling.[7,8] Optically pumped lasing as well as efficient light-emitting diodes (LEDs) have been demonstrated using perovskites.[9−13] While both strong and weak light−matter coupling have been demonstrated in different perovskite materials, they were mostly exemplified via photoluminescence measurements only.[14] The investigation of light−matter coupling in perovskite optoelectronic devices via absorption/emission combined with electrical and optical measurements in photovoltaic devices and light-emitting diodes, respectively, still remain scarce.[15,16] In principle, both weak and strong light−matter coupling can be achieved in a device having a configuration of thin-metal/semiconductor-stack/thick-metal. Precise control over the perovskite layer's thickness and roughness is required

Received: March 14, 2021
Published: June 18, 2021

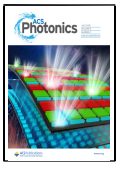

https://doi.org/10.1021/acsphotonics.1c00389
ACS Photonics 2021, 8, 2067−2073

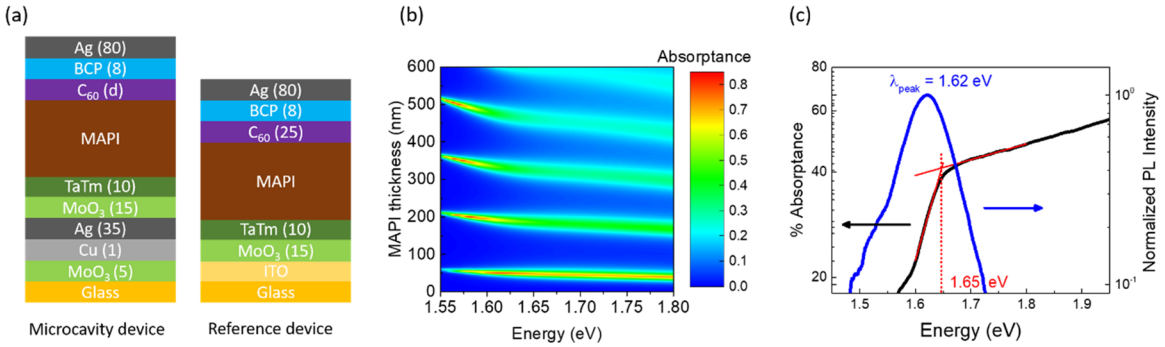

Figure 1. (a) Schematic of the layout of the microcavity and the reference devices. The number in the parentheses denotes the thickness of the corresponding layer in nm. (b) Transfer matrix method based simulated absorption of the MAPI layer in the microcavity device configuration shown in panel a, for increasing thicknesses of MAPI layer. (c) Absorptance and photoluminescence (PL) spectra of the coevaporated ∼195 nm MAPI film used for fabricating the microcavity and reference devices. The absorptance spectrum on the left of the dotted line (∼1.65 eV) marks the absorption-edge region.

for obtaining high-quality factor microcavities. A preparation process, therefore, must be employed that meets the above requirements. Vacuum deposition of perovskite leads to the formation of smooth and homogeneous films with a precise control over the film thickness and is therefore ideal for preparing perovskite films in the above microcavity device configuration.[17]

In this work, we investigate the microcavity effects (weak light-matter coupling) in vacuum deposited, p-i-n methylammonium lead iodide ($CH_3NH_3PbI_3$, MAPI) photovoltaic devices by integrating them into a planar Fabry-Pérot microcavity formed between two silver electrodes. We fine-tuned the position of the microcavity mode by modifying the thickness of electron transporting C_{60} layer. Tuning the microcavity mode to the absorption-edge region of MAPI enhances the absorption of the relatively low energy photons and steepens the absorption onset of the device. The microcavity devices do not suffer from significant additional voltage losses, and they exhibit a reduced effective optical gap compared to the control ITO-based device. Our study offers important guidelines for selecting the spectral position of the microcavity mode in perovskite based optoelectronic devices.

RESULTS AND DISCUSSION

Thermal evaporation under a pressure of $<1 \times 10^{-5}$ mbar was employed for the fabrication of complete MAPI based photovoltaic devices as it offers control over the film thickness, which is essential for the fine-tuning of the microcavity mode, and because it allows the fabrication of optically flat layers.[18] Microcavity devices and the control reference device on ITO were fabricated in the p-i-n configuration, as shown in Figure 1a, where TaTm and BCP are *N*4,*N*4,*N*4″,*N*4″-tetra([1,1′-biphenyl]-4-yl)-[1,1′:4′,1″-terphenyl]-4,4″-diamine and bathocuproine, respectively.

The optimum thicknesses of the charge transport layers in the ITO reference device were used as identified previously.[19] Silver (Ag) was used for fabricating both the semitransparent and the opaque reflecting electrodes. A thickness of 35 nm was selected for the semitransparent Ag electrode to achieve a strong microcavity effect and consequently a high absorption enhancement in the device. The absorption of light in the MAPI layer was simulated using the transfer matrix method to determine the microcavity absorption enhancement in the device for increasing thicknesses of MAPI (see Experimental Details). We note that, for the optical simulation, the thickness of the semitransparent electrode was set to 27 nm as the simulated transmittance of the corresponding Ag thin film matched well with the experimentally measured transmittance of the 35 nm Ag film (Figure S1a). This discrepancy is ascribed to the thickness and morphology dependence of the optical constants of Ag films.[20] From the simulation results (Figure 1b), it can be observed that microcavity absorption enhancement can occur over the entire low photon energy range of 1.55 to 1.80 eV for multiple thickness-ranges of the MAPI layer. The largest enhancement in the absorption, however, mostly occurs at energies below ∼1.65 eV where the absorption of the MAPI film is very low (Figure 1c). We, therefore, selected the above absorption-edge region for studying the effect of microcavity absorption enhancement on the photovoltaic performance of the devices. The first two ranges of MAPI thicknesses that lead to the microcavity formation in the above spectral region are approximately centered at 50 and 190 nm. As the thickness of MAPI in the first range is very low, we selected the second thickness-range for our studies.

The separation between the two light reflectors, which in our devices are the thick fully reflective, and the thinner semitransparent Ag electrode, influences the spectral position of the microcavity resonance in the device. Therefore, the distance between these two Ag electrodes must be systematically controlled to fine-tune the position of the microcavity mode across the MAPI absorption-edge. While the perovskite thickness can be reasonably well controlled when deposited through vacuum sublimation, it is not trivial to control its thickness with an accuracy down to 10 nm as it involves the sublimation and subsequent reaction of two precursors.[21] Hence, the tuning of the total stack thickness, and therefore of the microcavity mode is easier when done by modulating the thickness of either the hole transport material or the electron transport material. To ensure minimum side effects, such as an increase in the stack resistance, the C_{60} layer was selected to control the overall cavity length by a variation of its thickness (d) as it has a much higher carrier mobility than the hole transporting layer. Two microcavity devices were fabricated with an average MAPI layer thickness of 195 ± 5 nm and C_{60} thicknesses of 25 and 30 nm along with an ITO reference device having an equally thick MAPI layer and a fixed, 25 nm thickness of C_{60}. Figure 1c shows the photoluminescence spectrum and the absorptance spectrum marking the absorption-edge region of the 195 nm MAPI film.[7]

https://doi.org/10.1021/acsphotonics.1c00389
ACS Photonics 2021, 8, 2067−2073

To ensure that the microcavity devices employing the semitransparent Ag electrode effectively work as photovoltaic devices, we determine the current density−voltage (J−V) characteristics of the photovoltaic cells under simulated AM 1.5G illumination (Figure 2a and Table 1). Due to the reflective nature of the microcavity devices outside of the cavity-resonance spectrum, they show lower short-circuit current density (J_{sc}) than the ITO reference device. Importantly, we note that the J−V curves of all the microcavity devices exhibit neat rectification characteristics with a fill factor of >0.77, which is similar to that of the reference device (~0.76). This suggests the absence of any significant additional shunt and series resistance losses in the microcavity devices relative to the ITO reference device (this implies that the quality of the MAPI layer is similar on the semitransparent metal electrode as on ITO). The reference device efficiency is lower than what is usually obtained primarily due to the lower J_{sc} caused by the thinner MAPI layer. The 25 nm C_{60} device exhibits slightly higher J_{sc} than the 30 nm C_{60} based device due to the higher overlap between its external quantum efficiency (EQE, shown below in Figure 3) and the AM 1.5G spectra.

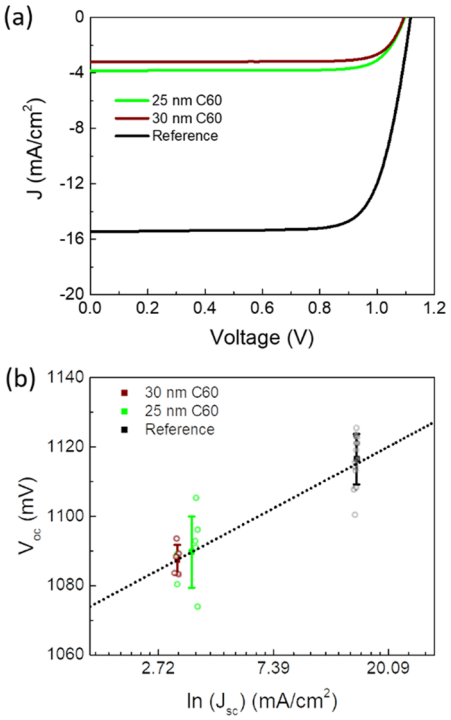

Figure 2. (a) Current density vs voltage scans for the reference and microcavity devices when illuminated with a simulated AM1.5G spectrum at an intensity of 100 mW/cm^2. (b) Plot of open circuit voltage (V_{oc}) vs the natural logarithm of short-circuit current density (J_{sc}) of the three devices. The average ($\ln(J_{sc})$,V_{oc}) coordinates of each device type (filled square symbol) is calculated from the data of 5 to 12 devices per type. The standard deviation in the V_{oc} and the individual (V_{oc}, J_{sc}) data points (open sphere symbols) of each type of device that were processed to obtain the above statistics are also shown. The dashed line is extrapolated from the average V_{oc}, $\ln(J_{sc})$ coordinates of the above two microcavity devices.

The open circuit voltage (V_{oc}) of the microcavity devices is lower than that observed for the reference device. The V_{oc} in any kind of solar cell increases linearly with ln (J_{sc}).[22] To verify that the reduced J_{sc} is the only reason for the lower V_{oc} in the microcavity devices, we extrapolate a line passing through the [V_{oc}, $\ln(J_{sc})$] coordinates of the microcavity devices (Figure 2b). We observe that the extrapolated V_{oc} value of the microcavity devices at the $\ln(J_{sc})$ coordinate of the reference device, is comparable to the observed V_{oc} value of the reference device. This implies that, at a similar current density, the V_{oc} of the microcavity devices would be very similar to that of the reference device, indicating the absence of any significant voltage losses in the former. Hence, the observed lower V_{oc} values of the microcavity devices with 25 and 30 nm C_{60} as compared to the reference device is exclusively due to their lower J_{sc} (due to their less transparent Ag front electrodes).

Having established that the microcavity devices behave similar as the reference device, albeit with a lower J_{sc}, we now investigate the effect of the microcavity on the spectral response of the devices. The measured external quantum efficiency (EQE) of the reference and the microcavity devices are displayed as a function of the excitation energy in Figure 3a. At high photon excitation energies, the microcavity devices exhibit a similar EQE spectral shape as that of the reference device. The lower EQE of the microcavity devices in the above spectrum is due to the low transparency of their front semitransparent Ag electrode compared to ITO. The main difference in the shape of their EQE occurs at photon energies below ~2 eV. While the EQE of the reference device first gradually decreases and then drops sharply upon reaching the band-edge, the microcavity devices exhibit an increase in the EQE at the band-edge region, leading to the formation of an intense and narrow peak (Figure 3a). Moreover, upon zooming in the spectra in the energy range of 1.55−1.70 eV, we find that the microcavity devices having 25 and 30 nm C_{60} show a slightly higher value of EQE than the reference device (Figure 3b). Furthermore, we observe a red-shift in the EQE peak positions of the microcavity devices with the increase in the thickness of the C_{60} layer. The EQE peak position in the devices having 25 and 30 nm C_{60} layer approximately lies at 1.633 and 1.623 eV, respectively. This successful modulation of the peak position in the EQE spectra verifies the existence of the microcavity effect in our devices. Moreover, the above microcavity peak positions match well with the position of the microcavity mode lying at 1.626 and 1.613 eV, respectively, in the devices (explained below).

Figure 3b shows the microcavity peak position of the three devices superimposed on the absorptance spectrum of the MAPI film. The simultaneous decrease in the absorptance of the MAPI film with the red-shift of the microcavity mode

Table 1. J−V Parameters of All the Photovoltaic Devices when Illuminated with a Simulated AM1.5G Spectrum at an Intensity of 100 mW/cm^2

device	V_{oc} (mV)	J_{sc} (mA/cm^2)	FF (%)	PCE (%)
reference ITO	1116 (±7.26)	15.23 (±0.13)	76.46 (±0.59)	13.01 (±0.18)
25 nm C_{60}	1090 (±10.28)	3.63 (±0.29)	79.50 (±2.26)	3.14 (±0.25)
30 nm C_{60}	1087 (±4.29)	3.20 (±0.05)	76.92 (±5.31)	2.68 (±0.15)

https://doi.org/10.1021/acsphotonics.1c00389
ACS Photonics 2021, 8, 2067−2073

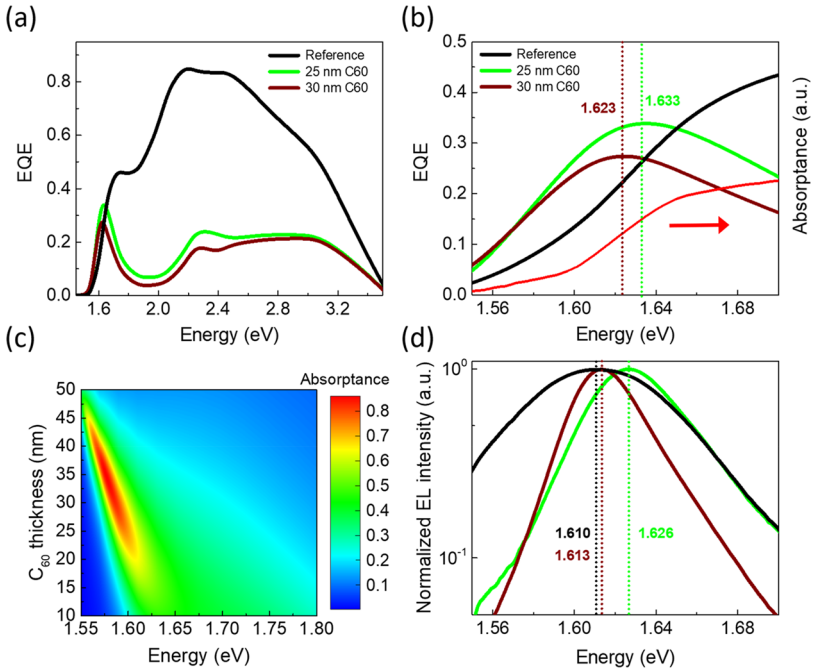

Figure 3. (a) External quantum efficiency (EQE) spectra of the reference and the microcavity devices. (b) Zoom-in of the EQE spectra of all the devices in the energy range of 1.55 to 1.7 eV, along with the absorptance spectrum of the fabricated ∼195 nm MAPI film (in arbitrary units, shown in light-red color). The dotted lines indicate the microcavity peak positions in the devices. (c) Transfer matrix method based simulated absorption of 195 nm MAPI layer in the microcavity architecture for increasing thicknesses of the C_{60} layer. (d) Normalized electroluminescence (EL) spectra of the microcavity and the reference devices when driven in forward bias. The vertical dotted lines indicate the peak positions of the EL spectrum of the devices.

increases the quality factor of the microcavity. As a result, the microcavity absorption peak becomes more narrow (i.e., the linewidth, or full width at half-maximum, decreases) as the C_{60} thickness increases.[23] The microcavity absorption enhancement is governed by the transfer of energy from the microcavity to MAPI via absorption. In the case of the device with a 25 nm C_{60} layer, the high-quality factor of the microcavity and the sufficiently high absorptance of the film allow an enhanced transfer of energy from the microcavity to MAPI, resulting in the highest enhancement of the EQE. The device with a 30 nm C_{60} layer exhibits a high quality microcavity, however, the reduced absorptance of the MAPI limits the transfer of energy of the microcavity to MAPI. Hence, in this device configuration, the enhancement of the EQE is only moderate. We note that the optical simulation result coincides with the observed trends of the microcavity absorption enhancement in MAPI. The simulation, however, predicts a smaller linewidth of the microcavity peaks for slightly higher thicknesses of C_{60} (∼27 nm to ∼37 nm). This minor discrepancy between simulated and experimental results is most likely caused by small deviations in the used values of the optical constants of MAPI film (Figure S1b). Additionally, small errors in the thickness determination may have also contributed to it.

The thickness of the semitransparent Ag electrode also affects the spectral response of the microcavity devices (Figure S3). We observe that the device with 20 nm Ag electrode exhibits a lower microcavity absorption enhancement and a wider-linewidth in the microcavity peak, compared to the device with a 40 nm Ag electrode. The use of a less reflecting 20 nm Ag electrode results in the formation of a low-quality factor microcavity which causes a smaller redistribution of the optical density of states, and hence a weak microcavity absorption enhancement in the device.

The electroluminescence (EL) spectrum of a photovoltaic cell can be observed when it is driven in forward bias.[24] The peak position in the EL spectrum of a microcavity diode closely corresponds to the position of the microcavity mode.[25] We, therefore, measure the EL spectrum of the microcavity devices along the normal direction and observe that the EL peak position or the microcavity mode in the devices having 25 and 30 nm thickness of C_{60} layer lie at 1.626, and 1.613 eV, respectively (Figure 3d). These EL peak positions are blue-shifted with respect to that of the reference device by 16 and 3 meV, respectively. The microcavity devices exhibit a relatively narrow-linewidth EL spectrum compared to the reference device. Moreover, the EL peak position of the three microcavity devices aligns well with the microcavity peak position of their corresponding EQE spectrum (Figure 3b,d). This further corroborates the existence of the microcavity effect in these devices. As a final proof of the existence of the microcavity, we performed angle-dependent EQE measurements for the device with a C_{60} layer of 25 nm. As shown in Figure S4 of the Supporting Information, the position of the microcavity mode blue shifts when the angle of incidence of the light with respect to the sample surface decreases, hence, again confirming the operation of the microcavity mode.

The effective optical gap (E_g) of all devices can be calculated as the maximum of the derivative of their EQE spectrum (d(EQE)/dE; Figure S2),[26] which corresponds to the energy of the lowest energy photons that can lead to a significant photocurrent.[27] We observe that the reference device and the microcavity devices with 25 and 30 nm C_{60} layer exhibit an E_g of 1.598, 1.582, and 1.577 eV, respectively. This indicates that the E_g values for these two microcavity devices are reduced

https://doi.org/10.1021/acsphotonics.1c00389
ACS Photonics 2021, 8, 2067−2073

with respect to the reference device. We recall that the lower V_{oc} of the microcavity devices was solely due to a reduced J_{sc} (Figure 2b). The V_{oc} deficit of a photovoltaic device is generally defined as $E_g/q - V_{oc}$, where q is the elementary charge. It quantifies the lower limit for the energy lost per absorbed photon, and hence, its reduction is highly desired for further improving the performance of photovoltaic devices. Hence, as the V_{oc} is equal to the reference device when corrected for the lower J_{sc} and the effective E_g is reduced, it implies that the V_{oc} deficit is reduced in these microcavity devices. Finally, we determine the Urbach energy of all the devices from their EQE tails (Figure S6),[28] which is an indication of the energetic-sharpness of the "band-edge" in a photovoltaic cell. We observe that the microcavity devices exhibit slightly lower Urbach energy values than the reference device, which may also contribute toward minimizing the V_{oc} deficit in MAPI-based photovoltaic cells.[29] To see the potential of these microcavity devices for photodetectors, the dark current was determined and is approximately one order of magnitude lower than that of the reference device at a bias of −1 V. We would like to stress, however, that the dark current can be further reduced by employing different charge injection layers, which is, however, outside the scope of this manuscript.

CONCLUSION

In conclusion, we demonstrated a facile, vacuum deposition-based method of integrating a perovskite photovoltaic device into a planar, metallic Fabry-Pérot microcavity. This method is easily extendable for fabricating perovskite based microcavity photodetectors and light-emitting diodes. Tuning the microcavity mode to the absorption-edge region of MAPI enhances the absorption of the relatively low energy photons and steepens the absorption onset, which reduces the E_g of the device. As a result, the V_{oc} deficit is reduced. We envisage that such a microcavity absorption enhancement in the weakly absorbing absorption-edge region could be exploited in multijunction devices via the employment of the microcavity device as a rear cell to further suppress the photon energy losses occurring in the low-energy spectrum.

EXPERIMENTAL DETAILS

Chemicals. MoO_3, bathocuproine (BCP), PbI_2, and methylammonium iodide (MAI) were purchased from Lumtec. *N*4,*N*4,*N*4′,*N*4′-tetra([1,1′-biphenyl]-4-yl)-[1,1′:4′,1′-terphenyl]-4,4′-diamine (TaTm) was provided by Novaled GmbH. Fullerene (C_{60}) was purchased from Sigma-Aldrich.

Fabrication of Reference ITO Device. Photolithographically patterned ITO-coated glass substrates were cleaned by following a standard procedure using soap, water, deionized water and isopropanol in a sonication bath, followed by UV treatment for 20 min. For device fabrication, the cleaned substrates samples were transferred to a nitrogen-filled glovebox (H_2O and O_2 < 0.1 ppm) containing the vacuum thermal evaporation chambers. All the films were thermally evaporated following the order of the stack of the photovoltaic devices (Figure 1a) in a pressure range of 10^{-6} mbar, at room temperature without any postannealing treatment. MoO_3 and TaTm were evaporated at the rate of 0.5 Å/s, while C_{60} and BCP were evaporated at a rate of 0.3 Å/s. Ag cathode was deposited at a rate of 0.4 and 1.0 Å/s for the initial 15 nm and the remaining 65 nm, respectively. MAPI film was grown by coevaporating PbI_2 and MAI. Thickness of all the organic and inorganic molecules were measured using quartz crystal microbalance (QCM) by applying calibration factors for each material. The latter was obtained by individually measuring the actual thickness of each layer deposited on glass using a mechanical profilometer (Ambios XP_1) and then comparing it with the corresponding value given by the QCM. The thickness of the coevaporated MAPI film was measured after the deposition using the profilometer.

Fabrication of the Microcavity Device. Glass substrates were cleaned similar to the patterned ITO substrates except that UV treatment was excluded. All the layers of the stack from MoO_3 to the Ag cathode were grown simultaneously, together with the ITO reference device. A 5 nm MoO_3 layer and 1 nm Cu seed layer were sequentially deposited on glass to minimize the reflection losses, and to enhance the adhesion and percolation of the above semitransparent Ag electrode, respectively.[3,30] The active area for the microcavity devices and the reference device was defined using a shadow mask and is equal to 0.05 cm^2.

Material and Device Characterization. Transfer matrix method based absorptance and transmittance simulations were performed using a home-built code integrated with the *tmm* package in a pyhton based IDE. The derivations of the formulas and calculations implemented to develop the *tmm* package can be found here.[31] The absorption and transmittance spectrum were measured using a fiber optics based Avantes Avaspec2048 Spectrometer. The photoluminescence spectrum was measured with an Avantes Avaspec2048 spectrometer and films were illuminated with a diode laser of integrated optics, emitting at 522 nm. The $J-V$ curves for the solar cells were recorded using a Keithley 2612A Source Meter in a −0.2 and 1.2 V voltage range, with 0.01 V steps and integrating the signal for 20 ms after a 10 ms delay, corresponding to a scan speed of about 0.3 V s^{-1}. The devices were illuminated under a Wavelabs Sinus 70 LED solar simulator. The light intensity was calibrated before every measurement using a calibrated Si reference diode.

For the EQE measurements, photocurrent response at different wavelength (measured with a white light halogen lamp in combination with band-pass filters) was measured, where the solar spectrum mismatch was corrected with a calibrated silicon reference cell (MiniSun simulator by ECN, from Netherlands). For the measurement of effective optical gap and Urbach energy of the microcavity and the reference photovoltaic devices in the main text, the devices were illuminated by a Quartz-Tungsten-Halogen lamp (Newport Apex 2-QTH) through a monochromator (Newport CS130-USB-3-MC), a chopper at 279 Hz and a focusing lens. The device current was measured as a function of energy from 3.5 to 1.5 eV in 0.02 eV steps using a lock-in amplifier (Stanford Research Systems SR830). In the peak region, the step size was reduced up to 0.005 eV to resolve the peaks properly. The system was calibrated and the solar spectrum mismatch was corrected using a calibrated Silicon reference cell. The Urbach energy was calculated from the linear fit of the slope of the exponential decay of the measured EQE spectrum of the devices.

ASSOCIATED CONTENT

Supporting Information

The Supporting Information is available free of charge at https://pubs.acs.org/doi/10.1021/acsphotonics.1c00389.

https://doi.org/10.1021/acsphotonics.1c00389
ACS Photonics 2021, 8, 2067−2073

Measured and simulated transmittance of thin Ag metal films, evaluation of the optical gap of the microcavity devices and EQE spectra for microcavity devices with different Ag electrode thicknesses, and Urbach energy determination from the EQE spectra (PDF)

AUTHOR INFORMATION

Corresponding Author

Henk J. Bolink − *Instituto de Ciencia Molecular, Universidad de Valencia, 46980 Paterna, Spain;* orcid.org/0000-0001-9784-6253; Email: henk.bolink@uv.es

Authors

Abhyuday Paliwal − *Instituto de Ciencia Molecular, Universidad de Valencia, 46980 Paterna, Spain*

Chris Dreessen − *Instituto de Ciencia Molecular, Universidad de Valencia, 46980 Paterna, Spain;* orcid.org/0000-0001-7444-6900

Kassio P. S. Zanoni − *Instituto de Ciencia Molecular, Universidad de Valencia, 46980 Paterna, Spain*

Benedikt Dänekamp − *Instituto de Ciencia Molecular, Universidad de Valencia, 46980 Paterna, Spain*

Beom-Soo Kim − *Instituto de Ciencia Molecular, Universidad de Valencia, 46980 Paterna, Spain*

Michele Sessolo − *Instituto de Ciencia Molecular, Universidad de Valencia, 46980 Paterna, Spain;* orcid.org/0000-0002-9189-3005

Koen Vandewal − *Institute for Materials Research (IMO-IMOMEC), Universiteit Hasselt, 3590 Diepenbeek, Belgium;* orcid.org/0000-0001-5471-383X

Complete contact information is available at: https://pubs.acs.org/10.1021/acsphotonics.1c00389

Notes

The authors declare no competing financial interest.

ACKNOWLEDGMENTS

The research leading to these results has received funding from the Spanish Ministry of Science, Innovation and Universities (MICIU, RTI2018-095362-A-I00, PCI2019-111829-2, CEX2019-000919-M, and EQC2018-004888-P) and the Comunitat Valenciana (IDIFEDER/2018/061 and PROMETEU/2020/077). C.D. acknowledges that the project that gave rise to these results received the support of a fellowship from "la Caixa" Foundation (ID 100010434, code LCF/BQ/DI19/11730020). M.S. acknowledges the MICIU for his RyC contract. A.P. acknowledges his Grisolia Grant from the Comunitat Valenciana GRISOLIAP/2020/134.

REFERENCES

(1) Vahala, K. J. Optical Microcavities. *Nature* **2003**, *424*, 839−846.

(2) Ebbesen, T. W. Hybrid Light-Matter States in a Molecular and Material Science Perspective. *Acc. Chem. Res.* **2016**, *49*, 2403−2412.

(3) Sergeant, N. P.; Hadipour, A.; Niesen, B.; Cheyns, D.; Heremans, P.; Peumans, P.; Rand, B. P. Design of Transparent Anodes for Resonant Cavity Enhanced Light Harvesting in Organic Solar Cells. *Adv. Mater.* **2012**, *24* (6), 728−732.

(4) Purcell, E. M. *Spontaneous Emission Probabilities at Radio Frequencies*; Springer: Boston, MA, 1995; pp 839−839, DOI: 10.1007/978-1-4615-1963-8_40.

(5) Siegmund, B.; Mischok, A.; Benduhn, J.; Zeika, O.; Ullbrich, S.; Nehm, F.; Böhm, M.; Spoltore, D.; Fröb, H.; Körner, C.; Leo, K.; Vandewal, K. Organic Narrowband Near-Infrared Photodetectors Based on Intermolecular Charge-Transfer Absorption. *Nat. Commun.* **2017**, *8* (1), 1−6.

(6) Jena, A. K.; Kulkarni, A.; Miyasaka, T. Halide Perovskite Photovoltaics: Background, Status, and Future Prospects. *Chem. Rev.* **2019**, *119* (5), 3036−3103.

(7) De Wolf, S.; Holovsky, J.; Moon, S. J.; Löper, P.; Niesen, B.; Ledinsky, M.; Haug, F. J.; Yum, J. H.; Ballif, C. Organometallic Halide Perovskites: Sharp Optical Absorption Edge and Its Relation to Photovoltaic Performance. *J. Phys. Chem. Lett.* **2014**, *5* (6), 1035−1039.

(8) Jiang, Y.; Wang, X.; Pan, A. Properties of Excitons and Photogenerated Charge Carriers in Metal Halide Perovskites. *Adv. Mater.* **2019**, *31* (47), 1806671.

(9) Xing, G.; Mathews, N.; Lim, S. S.; Yantara, N.; Liu, X.; Sabba, D.; Grätzel, M.; Mhaisalkar, S.; Sum, T. C. Low-Temperature Solution-Processed Wavelength-Tunable Perovskites for Lasing. *Nat. Mater.* **2014**, *13* (5), 476−480.

(10) Deschler, F.; Price, M.; Pathak, S.; Klintberg, L.; Jarausch, D. D.; Higler, R.; Huettner, S.; Leijtens, T.; Stranks, S. D.; Snaith, H. J.; Atature, M.; Phillips, R. T.; Friend, R. H. High Photoluminescence Efficiency and Optically-Pumped Lasing in Solution-Processed Mixed Halide Perovskite Semiconductors. *J. Phys. Chem. Lett.* **2014**, *5* (8), 1421−1426.

(11) Xu, W.; Hu, Q.; Bai, S.; Bao, C.; Miao, Y.; Yuan, Z.; Borzda, T.; Barker, A. J.; Tyukalova, E.; Hu, Z.; Kawecki, M.; Wang, H.; Yan, Z.; Liu, X.; Shi, X.; Uvdal, K.; Fahlman, M.; Zhang, W.; Duchamp, M.; Liu, J. M.; Petrozza, A.; Wang, J.; Liu, L. M.; Huang, W.; Gao, F. Rational Molecular Passivation for High-Performance Perovskite Light-Emitting Diodes. *Nat. Photonics* **2019**, *13* (6), 418−424.

(12) Jia, Y.; Kerner, R. A.; Grede, A. J.; Rand, B. P.; Giebink, N. C. Continuous-Wave Lasing in an Organic-Inorganic Lead Halide Perovskite Semiconductor. *Nat. Photonics* **2017**, *11* (12), 784−788.

(13) Sutherland, B. R.; Sargent, E. H. Perovskite Photonic Sources. *Nat. Photonics* **2016**, *10* (5), 295−302.

(14) Du, W.; Zhang, S.; Zhang, Q.; Liu, X. Recent Progress of Strong Exciton-Photon Coupling in Lead Halide Perovskites. *Adv. Mater.* **2019**, *31* (45), 1804894.

(15) Hanmandlu, C.; Liu, C. C.; Chen, C. Y.; Boopathi, K. M.; Wu, S. H.; Singh, M.; Mohapatra, A.; Lin, H. W.; Chang, Y. C. Y. C.; Chang, Y. C. Y. C.; Lai, C. S.; Chu, C. W. Top Illuminated Hysteresis-Free Perovskite Solar Cells Incorporating Microcavity Structures on Metal Electrodes: A Combined Experimental and Theoretical Approach. *ACS Appl. Mater. Interfaces* **2018**, *10* (21), 17973−17984.

(16) Miao, Y.; Cheng, L.; Zou, W.; Gu, L.; Zhang, J.; Guo, Q.; Peng, Q.; Xu, M.; He, Y.; Zhang, S.; Cao, Y.; Li, R.; Wang, N.; Huang, W.; Wang, J. Microcavity Top-Emission Perovskite Light-Emitting Diodes. *Light: Sci. Appl.* **2020**, *9*, 2047−7538.

(17) Ávila, J.; Momblona, C.; Boix, P. P.; Sessolo, M.; Bolink, H. J. Vapor-Deposited Perovskites: The Route to High-Performance Solar Cell Production? *Joule* **2017**, *1*, 431−442.

(18) Guillén, C.; Herrero, J. Surface-Properties Relationship in Sputtered Ag Thin Films: Influence of the Thickness and the Annealing Temperature in Nitrogen. *Appl. Surf. Sci.* **2015**, *324*, 245−250.

(19) Babaei, A.; Zanoni, K. P. S.; Gil-Escrig, L.; Pérez-Del-Rey, D.; Boix, P. P.; Sessolo, M.; Bolink, H. J. Efficient Vacuum Deposited P-I-N Perovskite Solar Cells by Front Contact Optimization. *Front. Chem.* **2020**, *7*, 936.

(20) Ding, G.; Clavero, C.; Schweigert, D.; Le, M. Thickness and Microstructure Effects in the Optical and Electrical Properties of Silver Thin Films. *AIP Adv.* **2015**, *5* (11), 117234.

(21) Kim, B. S.; Gil-Escrig, L.; Sessolo, M.; Bolink, H. J. Deposition Kinetics and Compositional Control of Vacuum-Processed CH3NH3PbI3Perovskite. *J. Phys. Chem. Lett.* **2020**, *11* (16), 6852−6859.

(22) Koster, L. J. A.; Mihailetchi, V. D.; Ramaker, R.; Blom, P. W. M. Light Intensity Dependence of Open-Circuit Voltage of Polymer:-Fullerene Solar Cells. *Appl. Phys. Lett.* **2005**, *86* (12), 123509.

(23) Lupton, J. M.; Koeppe, R.; Müller, J. G.; Feldmann, J.; Scherf, U.; Lemmer, U. Organic Microcavity Photodiodes. *Adv. Mater.* **2003**, *15* (17), 1471−1474.
(24) Gil-Escrig, L.; Longo, G.; Pertegás, A.; Roldán-Carmona, C.; Soriano, A.; Sessolo, M.; Bolink, H. J. Efficient Photovoltaic and Electroluminescent Perovskite Devices. *Chem. Commun.* **2015**, *51* (3), 569−571.
(25) Xiang, C.; Koo, W.; So, F.; Sasabe, H.; Kido, J. A Systematic Study on Efficiency Enhancements in Phosphorescent Green, Red and Blue Microcavity Organic Light Emitting Devices. *Light: Sci. Appl.* **2013**, *2*, e74.
(26) Rau, U.; Blank, B.; Müller, T. C. M.; Kirchartz, T. Efficiency Potential of Photovoltaic Materials and Devices Unveiled by Detailed-Balance Analysis. *Phys. Rev. Appl.* **2017**, *7* (4), 044016.
(27) Vandewal, K.; Benduhn, J.; Nikolis, V. C. How to Determine Optical Gaps and Voltage Losses in Organic Photovoltaic Materials. *Sustainable Energy and Fuels*; Royal Society of Chemistry, March 1, 2018; pp 538−544, DOI: 10.1039/c7se00601b.
(28) Gil-Escrig, L.; Dreessen, C.; Palazon, F.; Hawash, Z.; Moons, E.; Albrecht, S.; Sessolo, M.; Bolink, H. J. Efficient Wide-Bandgap Mixed-Cation and Mixed-Halide Perovskite Solar Cells by Vacuum Deposition. *ACS Energy Lett.* **2021**, *6* (2), 827−836.
(29) Ledinsky, M.; Schönfeldová, T.; Holovský, J.; Aydin, E.; Hájková, Z.; Landová, L.; Neyková, N.; Fejfar, A.; De Wolf, S. Temperature Dependence of the Urbach Energy in Lead Iodide Perovskites. *J. Phys. Chem. Lett.* **2019**, *10* (6), 1368−1373.
(30) Formica, N.; Ghosh, D. S.; Carrilero, A.; Chen, T. L.; Simpson, R. E.; Pruneri, V. Ultrastable and Atomically Smooth Ultrathin Silver Films Grown on a Copper Seed Layer. *ACS Appl. Mater. Interfaces* **2013**, *5* (8), 3048−3053.
(31) Peumans, P.; Yakimov, A.; Forrest, S. R. Small Molecular Weight Organic Thin-Film Photodetectors and Solar Cells. *J. Appl. Phys.* **2003**, *93*, 3693−3723.

https://doi.org/10.1021/acsphotonics.1c00389
ACS Photonics 2021, 8, 2067−2073